

1           **Contrasting interannual atmospheric CO<sub>2</sub> variabilities and their**  
2                           **terrestrial mechanisms for two types of El Niños**

3           Jun Wang<sup>1,2</sup>, Ning Zeng<sup>2,3</sup>, Meirong Wang<sup>4</sup>, Fei Jiang<sup>1</sup>, Jingming Chen<sup>1,5</sup>, Pierre  
4           Friedlingstein<sup>6</sup>, Atul K. Jain<sup>7</sup>, Ziqiang Jiang<sup>1</sup>, Weimin Ju<sup>1</sup>, Sebastian Lienert<sup>8,9</sup>, Julia  
5           Nabel<sup>10</sup>, Stephen Sitch<sup>11</sup>, Nicolas Viovy<sup>12</sup>, Hengmao Wang<sup>1</sup>, Andrew J. Wiltshire<sup>13</sup>

6           <sup>1</sup>International Institute for Earth System Science, Nanjing University, Nanjing, China

7           <sup>2</sup>State Key Laboratory of Numerical Modelling for Atmospheric Sciences and Geophysical Fluid  
8           Dynamics, Institute of Atmospheric Physics, Beijing, China

9           <sup>3</sup>Department of Atmospheric and Oceanic Science and Earth System Science Interdisciplinary  
10          Center, University of Maryland, College Park, Maryland, USA

11          <sup>4</sup>Joint Center for Data Assimilation Research and Applications/Key Laboratory of Meteorological  
12          Disaster of Ministry of Education, Nanjing University of Information Science & Technology,  
13          Nanjing, China

14          <sup>5</sup>Department of Geography, University of Toronto, Ontario M5S3G3, Canada

15          <sup>6</sup>College of Engineering, Mathematics and Physical Sciences, Unvernity of Exeter, Exeter EX4  
16          4QE, UK

17          <sup>7</sup>Department of Atmosheric Sciences, University of Illinois at Urbana-Champaign, Urbana, IL  
18          61801, USA

19          <sup>8</sup>Climate and Environmental Physics, Physics Institute, University of Bern, Bern, Switzerland

20          <sup>9</sup>Oeschger Centre for Climate Change Research, University of Bern, Bern, Switzerland

21          <sup>10</sup>Land in the Earth System, Max Planck Institute for Meteorology, D-20146 Hamburg, Germany

22          <sup>11</sup>College of Life and Environmental Sciences, University of Exeter EX4 4QF, UK

23          <sup>12</sup>Laboratoire des Sciences du Climat et de l'Environnement, LSCE/IPSL-CEA-CNRS-UVQS,  
24          F-91191, Gif sur Yvette, France

25          <sup>13</sup>Met office Hadley Centre, Fitzroy Rd, Exeter. EX1 3PB. UK

26  
27          **Correspondence to: (Ning Zeng, zeng@umd.edu; Fei Jiang, jiangf@nju.edu.cn)**

28

29 **Abstract**

30 El Niño has two different flavors, eastern Pacific (EP) and central Pacific (CP) El  
31 Niños, with different global teleconnections. However, their different impacts on the  
32 interannual carbon cycle variability remain unclear. We here compared the behaviors  
33 of interannual atmospheric CO<sub>2</sub> variability and analyzed their terrestrial mechanisms  
34 during these two types of El Niños, based on the Mauna Loa (MLO) CO<sub>2</sub> growth rate  
35 (CGR) and the Dynamic Global Vegetation Model's (DGVM) historical simulations.  
36 The composite analysis showed that evolution of the MLO CGR anomaly during EP  
37 and CP El Niños had three clear differences: (1) negative and neutral precursors in the  
38 boreal spring during an El Niño-developing year (denoted as “yr0”), (2) strong and  
39 weak amplitudes, and (3) durations of the peak from December (yr0) to April during  
40 an El Niño-decaying year (denoted as “yr1”) and from October (yr0) to January (yr1),  
41 respectively. The global land-atmosphere carbon flux ( $F_{TA}$ ) simulated by  
42 multi-models was able to capture the essentials of these characteristics. We further  
43 found that the gross primary productivity (GPP) over the tropics and the extratropical  
44 southern hemisphere (Trop+SH) generally dominated the global  $F_{TA}$  variations during  
45 both El Niño types. Regional analysis showed that during EP El Niño events  
46 significant anomalous carbon uptake caused by increased precipitation and colder  
47 temperatures, corresponding to the negative precursor, occurred between 30°S and  
48 20°N from January (yr0) to June (yr0). The strongest anomalous carbon releases,  
49 largely due to the reduced GPP induced by low precipitation and warm temperatures,  
50 occurred between the equator and 20°N from February (yr1) to August (yr1). In  
51 contrast, during CP El Niño events, clear carbon releases existed between 10°N and  
52 20°S from September (yr0) to September (yr1), resulting from the widespread dry and  
53 warm climate conditions. Different spatial patterns of land temperatures and

54 precipitation in different seasons associated with EP and CP El Niños accounted for  
55 the evolutionary characteristics of GPP, terrestrial ecosystem respiration (TER), and  
56 the resultant  $F_{TA}$ . Understanding these different behaviors of interannual atmospheric  
57  $CO_2$  variability, along with their terrestrial mechanisms during EP and CP El Niños, is  
58 important because the CP El Niño occurrence rate might increase under global  
59 warming.

60

## 61 **1 Introduction**

62 The El Niño–Southern Oscillation (ENSO), a dominant year-to-year climate variation,  
63 leads to a significant interannual variability in the atmospheric  $CO_2$  growth rate (CGR)  
64 (Bacastow, 1976; Keeling et al., 1995). Many studies, including measurement  
65 campaigns (Lee et al., 1998; Feely et al., 2002), atmospheric inversions (Bousquet et  
66 al., 2000; Peylin et al., 2013), and terrestrial carbon cycle models (Zeng et al., 2005;  
67 Wang et al., 2016), have consistently suggested the dominant role of terrestrial  
68 ecosystems, especially tropical ecosystems, in contributing to interannual atmospheric  
69  $CO_2$  variability. Recently, Ahlstrom et al. (2015) further suggested ecosystems over  
70 the semi-arid regions played the most important role in the interannual variability of  
71 the land  $CO_2$  sink. Moreover, this ENSO-related interannual carbon cycle variability  
72 may be enhanced under global warming, with approximately a 44% increase in the  
73 sensitivity of terrestrial carbon flux to ENSO (Kim et al., 2017).

74 Tropical climatic variations (especially in surface air temperature and precipitation)  
75 induced by ENSO and plant and soil physiological responses can largely account for  
76 interannual terrestrial carbon cycle variability (Zeng et al., 2005; Wang et al., 2016;  
77 Jung et al., 2017). Multi-model simulations involved in the TRENDY project and the  
78 Coupled Model Intercomparison Project Phase 5 (CMIP5) have consistently

79 suggested the biological dominance of gross primary productivity (GPP) or net  
80 primary productivity (NPP) (Kim et al., 2016; Wang et al., 2016; Piao et al., 2013;  
81 Ahlstrom et al., 2015). However, debates continue regarding which is the dominant  
82 climatic mechanism (temperature or precipitation) in the interannual variability of the  
83 terrestrial carbon cycle (Wang et al., 2013; Wang et al., 2014; Cox et al., 2013; Zeng  
84 et al., 2005; Ahlstrom et al., 2015; Wang et al., 2016; Qian et al., 2008; Jung et al.,  
85 2017).

86 The atmospheric CGR or land–atmosphere carbon flux ( $F_{TA}$  – if this is positive, this  
87 indicates a flux into the atmosphere) can anomalously increase during El Niño, and  
88 decrease during La Niña episodes (Zeng et al., 2005; Keeling et al., 1995). Cross  
89 correlation analysis shows that atmospheric CGR and  $F_{TA}$  lags the ENSO by several  
90 months (Qian et al., 2008; Wang et al., 2013; Wang et al., 2016). This is due to the  
91 period needed for surface energy and soil moisture adjustment following  
92 ENSO-related circulation and precipitation anomalies (Gu and Adler, 2011; Qian et al.,  
93 2008). However, considering the variability inherent in the ENSO phenomenon  
94 (Capotondi et al., 2015), the atmospheric CGR and  $F_{TA}$  can show different behaviors  
95 during different El Niño events (Schwalm, 2011; Wang et al., 2018).

96 El Niño events can be classified into eastern Pacific El Niño (EP El Niño, also termed  
97 as conventional El Niño) and central Pacific El Niño (CP El Niño, also termed as El  
98 Niño Modoki) according to the patterns of sea-surface warming over the tropical  
99 Pacific (Ashok et al., 2007; Ashok and Yamagata, 2009). These two types of El Niño  
100 have different global climatic teleconnections, associated with contrasting climate  
101 conditions in different seasons (Weng et al., 2007; Weng et al., 2009). For example,  
102 positive winter temperature anomalies are located mostly over the northeastern US  
103 during an EP El Niño, while warm anomalies occur in the northwestern US during a

104 CP El Niño (Yu et al., 2012). The contrasting summer and winter precipitation  
105 anomaly patterns associated with these two El Niño events over the China, Japan, and  
106 the US were also discussed by Weng et al. (2007; 2009). Importantly, Ashok et al.  
107 (2007) suggested that the occurrence of the CP El Niño had increased during recent  
108 decades compared to the EP El Niño. This phenomenon can probably be attributed to  
109 the anthropogenic global warming (Ashok and Yamagata, 2009; Yeh et al., 2009).  
110 However, the contrasting impacts of EP and CP El Niño events on carbon cycle  
111 variability remain unclear. In this study, we attempt to reveal their different impacts.  
112 We compared the behavior of interannual atmospheric CO<sub>2</sub> variability and analyzed  
113 their terrestrial mechanisms corresponding to these two types of El Niños, based on  
114 Mauna Loa long-term CGR and TRENDY multi-model simulations.  
115 This paper is organized as follows: section 2 describes the datasets used, methods, and  
116 TRENDY models selected. Section 3 reports the results regarding the relationship  
117 between ENSO and CGR and EP and CP El Niño events, in addition to a composite  
118 analysis on carbon cycle behaviors, and terrestrial mechanisms. Section 4 contains a  
119 discussion of the results, and section 5 presents concluding remarks.

120

## 121 **2 Datasets and Methods**

### 122 **2.1 Datasets used**

123 Data for monthly atmospheric CO<sub>2</sub> concentrations between 1960 and 2013 was  
124 collected from the National Oceanic and Atmospheric Administration (NOAA) Earth  
125 System Research Laboratory (ESRL). The annual CO<sub>2</sub> growth rate (CGR) in Pg C  
126 yr<sup>-1</sup> was derived month by month according to the approach described by Patra et al.,  
127 (2005) and Sarmiento et al. (2010). The calculation is as follows:

128 
$$CGR(t) = \gamma \cdot [pCO_2(t + 6) - pCO_2(t - 6)] \quad (1)$$

129 where  $\gamma = 2.1276 \text{ Pg C ppm}^{-1}$ ;  $pCO_2$  is the atmospheric partial pressure of  $CO_2$  in  
130 ppm; and  $t$  is the time in months. The detailed calculation of the conversion factor,  $\gamma$ ,  
131 can be found in the appendix (Sarmiento et al., 2010).

132 Temperature and precipitation datasets for 1960 through 2013 were obtained from  
133 CRUNCEPv6 (Wei et al., 2014). CRUNCEP datasets are the merged product of  
134 ground observation-based CRU data and model-based NCEP-NCAR Reanalysis data  
135 with a  $0.5^\circ \times 0.5^\circ$  spatial resolution and 6-hour temporal resolution. These datasets  
136 are consistent with the climatic forcing used to run dynamic global vegetation models  
137 in TRENDY v4 (Sitch et al., 2015). The sea surface temperature anomalies (SSTA)  
138 over the Niño3.4 region ( $5^\circ\text{S}$ – $5^\circ\text{N}$ ,  $120^\circ$ – $170^\circ\text{W}$ ) were obtained from the NOAA’s  
139 Extended Reconstructed Sea Surface Temperature (ERSST) dataset, version 4 (Huang  
140 et al., 2015).

141 The inversion of  $F_{TA}$  from the Jena CarboScope was used for comparison with the  
142 TRENDY multi-model simulations from 1981 to 2013. The Jena CarboScope Project  
143 provided the estimates of the surface-atmosphere carbon flux based on atmospheric  
144 measurements using an “atmospheric transport inversion”. The inversion run used  
145 here was s81\_v3.8 (Rodenbeck et al., 2003).

146

## 147 **2.2 TRENDY simulations**

148 We analyzed eight state-of-the-art dynamic global vegetation models from TRENDY

149 v4 for the period 1960–2013: CLM4.5 (Oleson et al., 2013), ISAM (Jain et al., 2013),  
150 JSBACH (Reick et al., 2013), JULES (Clark et al., 2011), LPX-Bern (Keller et al.,  
151 2017), OCN (Zaehle and Friend, 2010), VEGAS (Zeng et al., 2005), and VISIT (Kato  
152 et al., 2013) (Table 1). Since LPX-Bern was excluded in the analysis of TRENDY v4,  
153 due to it not fulfilling the minimum performance requirement, the output over the  
154 same time period of a more recent version (LPX-Bern v1.3) was used. These models  
155 were forced using a common set of climatic datasets (CRUNCEPv6), and followed  
156 the same experimental protocol. The ‘S3’ run was used in this study, in which  
157 simulations forced by all the drivers including CO<sub>2</sub>, climate, land use, and land cover  
158 change (Sitch et al., 2015).

159 The simulated terrestrial variables (NBP, GPP, TER, soil moisture, and others) were  
160 interpolated into a consistent 0.5°×0.5° resolution using the first-order conservative  
161 remapping scheme (Jones, 1999) by Climate Data Operators (CDO):

$$162 \quad \overline{F}_k = \frac{1}{A_k} \int f dA \quad (2)$$

163 where  $\overline{F}_k$  denotes the area-averaged destination quantity;  $A_k$  is the area of cell  $k$ ;  
164 and  $f$  is the quantity in an old grid which has overlapping area with the destination  
165 grid. Then the median, 5%, and 95% percentiles of the multi-model simulations were  
166 calculated grid by grid to study the different effects of EP and CP El Niños on  
167 terrestrial carbon cycle interannual variability.

168

169

170 **2.3 El Niño criterion and classification methods**

171 El Niño events are determined by the Oceanic Niño Index (ONI) [i.e. the running  
172 3-month mean SST anomaly over the Niño3.4 region]. This NOAA criterion is that El  
173 Niño events are defined as 5 consecutive overlapping 3-month periods at or above the  
174  $+0.5^\circ$  anomaly.

175 We classified El Niño events into EP or CP based on the consensus of three different  
176 identification methods directly adopted from a previous study (Yu et al., 2012). These  
177 identification methods included the El Niño Modoki Index (EMI) (Ashok et al., 2007),  
178 the EP/CP-index method (Kao and Yu, 2009), and the Niño method (Yeh et al., 2009).

179

180 **2.4 Anomaly calculation and composite analysis**

181 To calculate the anomalies, we first removed the long-term climatology for the period  
182 from 1960 to 2013 from all of the variables used here, in order to eliminate seasonal  
183 cycle. We then detrended them based on a linear regression, because (1) the trend in  
184 terrestrial carbon variables was mainly caused by long-term CO<sub>2</sub> fertilization and  
185 climate change, and (2) the trend in CGR primarily resulted from the anthropogenic  
186 emissions. We used these detrended monthly anomalies to investigate the impacts of  
187 El Niño events on the interannual carbon cycle variability.

188 More specifically, in terms of the composite analysis, we calculated the averages of  
189 the carbon flux anomaly (CGR,  $F_{TA}$  i.e.) during the selected EP and CP El Niño  
190 events, respectively. We use the Bootstrap Methods (Mudelsee, 2010) to estimate the  
191 95% confidence intervals and the Student's *t*-test to estimate the significance levels  
192 in the composite analysis. An 80% significance level was selected, as per Weng et al.

193 (2007), due to the limited number of EP El Niño events.

194

### 195 **3 Results**

#### 196 **3.1 The relationship between ENSO and interannual atmospheric CO<sub>2</sub>** 197 **variability**

198 The interannual atmospheric CO<sub>2</sub> variability closely coupled with ENSO (Fig. 1) with  
199 noticeable increases in CGR during El Niño and decreases during La Niña,  
200 respectively (Bacastow, 1976; Keeling and Revelle, 1985). The correlation coefficient  
201 between the MLO CGR and the Niño3.4 Index from 1960 to 2013 was 0.43 ( $p <$   
202 0.01). A regression analysis further indicated that a per unit increase in the Niño3.4  
203 Index can lead to a 0.60 Pg C yr<sup>-1</sup> increase in the MLO CGR.

204 The variation in the global F<sub>TA</sub> anomaly simulated by TRENDY models resembled the  
205 MLO CGR variation, with a correlation coefficient of 0.54 ( $p < 0.01$ ; Fig. 1b). This  
206 was close to the correlation coefficient of 0.61 ( $p < 0.01$ ; Fig. 1b) between the MLO  
207 CGR and the Jena CarboScope s81 for the time period from 1981 to 2013. This  
208 indicates that the terrestrial carbon cycle can largely explain the interannual  
209 atmospheric CO<sub>2</sub> variability, as suggested by previous studies (Bousquet et al., 2000;  
210 Zeng et al., 2005; Peylin et al., 2013; Wang et al., 2016). Moreover, the correlation  
211 coefficient of the TRENDY global F<sub>TA</sub> and the Niño3.4 Index reached 0.49 ( $p <$   
212 0.01), and a similar regression analysis of F<sub>TA</sub> with Niño3.4 showed a sensitivity of  
213 0.64 Pg C yr<sup>-1</sup> K<sup>-1</sup>. However, owing to the diffuse light fertilization effect induced by  
214 the eruption of Mount Pinatubo in 1991 (Mercado et al., 2009), the Jena CarboScope

215 s81 indicated that the terrestrial ecosystems had an anomalous uptake during the  
216 1991/92 El Niño event, making the MLO CGR an anomalous decrease. However,  
217 TRENDY models did not capture this phenomenon. This was not only due to a lack of  
218 a corresponding process representation in some models, but also because the  
219 TRENDY protocol did not include diffuse and direct light forcing.

220

### 221 **3.2 EP and CP El Niño events**

222 Schematic diagrams of the two types of El Niños (EP and CP) are shown in Fig. 2.  
223 During EP El Niño events (Fig. 2a), a positive sea surface temperature anomaly  
224 (SSTA) occurs in the eastern equatorial Pacific Ocean, showing a dipole SSTA pattern  
225 with the positive zonal SST gradient. This condition forms a single cell of Walker  
226 circulation over the tropical Pacific, with a dry downdraft in the western Pacific and  
227 wet updraft in the central-eastern Pacific. In contrast, an anomalous warming in the  
228 central Pacific, sandwiched by anomalous cooling in the east and west, is observed  
229 during CP El Niño events (Fig. 2b). This tripole SSTA pattern makes the  
230 positive/negative zonal SST gradient in the western/eastern tropical Pacific, resulting  
231 in an anomalous two-cell Walker circulation over the tropical Pacific. This alteration  
232 in atmospheric circulation produces a wet region in the central Pacific. Moreover,  
233 apart from these differences in the equatorial Pacific, the SSTA in other oceanic  
234 regions also differ remarkably (Weng et al., 2007; Weng et al., 2009).

235 Based on the NOAA criterion, a total of 17 El Niño events were detected from 1960  
236 through 2013. The events were then categorized into an EP or a CP El Niño based on

237 a consensus of three identification methods (EMI, EP/CP-index, and Niño methods)  
238 (Yu et al., 2012). Considering the effect of diffuse radiation fertilization induced by  
239 volcano eruptions (Mercado et al., 2009), we removed the 1963/64, 1982/83, and  
240 1991/92 El Niño events, in which Mount Agung, El Chichón, and Pinatubo erupted,  
241 respectively. In addition, we closely examined those extended El Niño events that  
242 occurred in 1968/70, 1976/78, and 1986/88. Based on the typical responses of MLO  
243 CGR to El Niño events (anomalous increase lasting from the El Niño developing year  
244 to El Niño decaying year; Supplementary Fig. S1), we retained 1968/69, 1976/77, and  
245 1987/88 El Niño periods. Finally, we got 4 EP El Niño and 7 CP El Niño events in  
246 this study (Table 2; Fig. 1b), with the composite SSTA evolutions as shown in  
247 Supplementary Fig. S2.

248

### 249 **3.3 Responses of atmospheric CGR to two types of El Niños**

250 Based on the selected EP and CP El Niño events, a composite analysis was conducted  
251 with the non-smoothed detrended monthly anomalies of the MLO CGR and the  
252 TRENDY global  $F_{TA}$  to reveal the contrasting carbon cycle responses to these two  
253 types of El Niños (Fig. 3). In addition to the differences in the location of anomalous  
254 SST warming and the alteration of the atmospheric circulation in EP and CP El Niños  
255 shown in Fig. 2, the following findings were elucidated: (1) different El Niño  
256 precursors: the SSTA was significantly negative in EP El Niño during the boreal  
257 winter (JF) and spring (MAM) in yr0 (hereafter yr0 and yr1 refer to the El Niño  
258 developing and decaying year, respectively). Conversely, the SSTA was neutral in CP

259 El Niño; (2) different tendencies of SST ( $\partial SST / \partial t$ ): the tendency of SST in EP El  
260 Niño was stronger than that in CP El Niño; (3) different El Niño amplitudes: due to  
261 the different tendencies of SST, the amplitude of EP El Niño was basically stronger  
262 than that of CP El Niño, though they all reached maturity in November or December  
263 of yr0 (Figs. 3a and 3c).

264 Correspondingly, behaviors of the MLO CGR during these two types of El Niño  
265 events also displayed some differences (Figs. 3b and 3d). During EP El Niño events  
266 (Fig. 3b), the MLO CGR was negative in boreal spring (yr0) and increased quickly  
267 from boreal fall (yr0), whereas it was neutral in boreal spring (yr0) and slowly  
268 increases from boreal summer (yr0) during the CP El Niño episode (Fig. 3d). The  
269 amplitude of the MLO CGR anomaly during EP El Niño events was generally larger  
270 than that during CP El Niño events. Importantly, the duration of the MLO CGR peak  
271 during EP El Niño was from December (yr0) to April (yr1), while the MLO CGR  
272 anomaly peaked from October (yr0) to January (yr1) during CP El Niño. We here  
273 simply defined the peak duration as the period above the 75% of the maximum CGR  
274 (or  $F_{TA}$ ) anomaly, in which the variabilities of less than 3 months below the threshold  
275 were also included. The positive MLO CGR anomaly ended around September (yr1)  
276 in both cases (Figs. 3b and 3d). During the finalization of this paper, we noted the  
277 publication of Chylek et al. (2018) who also found CGR amplitude difference in  
278 response to the two types of events.

279 A comparison of the MLO CGR with the TRENDY global  $F_{TA}$  anomalies (Figs. 3b

280 and 3d) indicated that the TRENDY global  $F_{TA}$  effectively captured the characteristics  
281 of CGR evolution during the CP El Niño. In contrast, the amplitude of the TRENDY  
282 global  $F_{TA}$  anomaly was somewhat underestimated during the EP El Niño, causing a  
283 lower statistical significance (Fig. 3b). This underestimation of the global  $F_{TA}$   
284 anomaly can, for example, be clearly seen in a comparison between the TRENDY and  
285 the Jena CarboScope during the extreme 1997/98 EP El Niño (Fig. 1b). Also, other  
286 characteristics can be basically captured. Therefore, insight into the mechanisms of  
287 these CGR evolutions during EP and CP El Niños, based on the simulations by  
288 TRENDY models, is still possible.

289

### 290 **3.4 Regional contributions, characteristics, and their mechanisms**

291 We separated the TRENDY global  $F_{TA}$  anomaly by major geographic regions into two  
292 parts: the extratropical northern hemisphere (NH, 23°N–90°N), and the tropics plus  
293 extratropical southern hemisphere (Trop+SH, 60°S–23°N) (Fig. 4). In a comparison of  
294 the contributions from these two parts, it was found that the  $F_{TA}$  over Trop+SH played  
295 a more important role in the global  $F_{TA}$  anomaly in both cases (Figs. 4b and 4d), and  
296 this finding was consistent with previous studies (Bousquet et al., 2000; Peylin et al.,  
297 2013; Zeng et al., 2005; Wang et al., 2016; Ahlstrom et al., 2015; Jung et al., 2017).  
298 The  $F_{TA}$  over Trop+SH was negative in austral fall (MAM; yr0), increased from  
299 austral spring (SON; yr0), and peaked from December (yr0) to April (yr1) during the  
300 EP El Niño (Fig. 4b). Conversely, it was nearly neutral in austral fall (yr0), increased  
301 from austral winter (JJA; yr0), and peaked from November (yr0) to March (yr1)

302 during the CP El Niño (Fig. 4d). These evolutionary characteristics in the  $F_{TA}$  over the  
303 Trop+SH were generally consistent with the global  $F_{TA}$  and the MLO CGR (Figs. 3b  
304 and 3d). In contrast, the contributions from the  $F_{TA}$  anomaly over the NH were  
305 relatively weaker (or nearly neutral) (Figs. 4a and 4c).

306 According to the equation  $F_{TA} = -NBP = TER - GPP + D$  (where  $D$  is the carbon  
307 flux caused by the disturbances such as the wildfires, harvests, grazing, land cover  
308 change etc.), the variation in  $F_{TA}$  can be explained by the variations in GPP, TER, and  
309  $D$ . The  $D$  simulated by TRENDY was nearly neutral during both El Niño types (Fig.  
310 4). Therefore, GPP and TER largely accounted for the variation in  $F_{TA}$ .

311 More Specifically, in Trop+SH, GPP anomalies dominated the variations in  $F_{TA}$  for  
312 both El Niño types, but their evolutions differed (Figs. 4b and 4d). The GPP showed  
313 an anomalous positive value during austral fall (yr0), and an anomalous negative  
314 value from austral fall (yr1) to winter (yr1), with the minimum around April (yr1)  
315 during the EP El Niño (Fig. 4b). Conversely, the GPP anomaly was always negative,  
316 with the minimum occurring around October or November (yr0) during the CP El  
317 Niño (Fig. 4d). The variation in the TER in both El Niños was relatively weaker than  
318 that of the GPP (Figs. 4b and d). The anomalous positive TER during austral spring  
319 (yr0) and summer (yr1) accounted for the increase in  $F_{TA}$ , and it partly canceled the  
320 negative GPP in austral fall (yr1) and winter (yr1) during the EP El Niño (Fig. 4b). In  
321 contrast, the TER had a reduction in yr0 during the CP El Niño (Fig. 4d). Over the  
322 NH, though the  $F_{TA}$  anomaly was relatively weaker, the behaviors of GPP and TER

323 differed in EP and CP El Niños. GPP and TER consistently decreased in the growing  
324 season of yr0 and increased in the growing season of yr1 during the EP El Niño (Fig.  
325 4a), whereas they only showed some increase during boreal summer (yr1) during the  
326 CP El Niño (Fig. 4c).

327 These evolutionary characteristics of GPP, TER, and the resultant  $F_{TA}$  principally  
328 resulted from their responses to the climate variability. Figure 5 shows the  
329 standardized observed surface air temperature, precipitation, and TRENDY simulated  
330 soil moisture contents. Over the Trop+SH, taking into consideration the regulation of  
331 thermodynamics and hydrological cycle on surface energy balance, variations in  
332 temperature and precipitation (soil moisture) were always opposite during the two  
333 types of El Niños (Figs. 5b and d). Additionally, adjustments in soil moisture lagged  
334 precipitation by approximately 2–4 months, owing to the so-called ‘soil memory’ of  
335 water recharge (Qian et al., 2008). The variations in GPP in both the El Niño types  
336 were closely associated with variations in soil moisture, namely water availability  
337 largely dominated by precipitation (Figs. 4b and 4d and 5b and 5d), and this result  
338 was consistent with previous studies (Zeng et al., 2005; Zhang et al., 2016). Warm  
339 temperatures during El Niño episodes can enhance the ecosystem respiration, but dry  
340 conditions can reduce it. These cancellations from warm and dry conditions made the  
341 amplitude of TER variation smaller than that of GPP (Figs. 4b and 4d). Over the NH,  
342 variations in temperature and precipitation were basically in the same direction (Figs.  
343 5a and 5c), as opposed to their behaviors over the Trop+SH. This was due to the

344 different climatic dynamics of the two regions (Zeng et al., 2005). During the EP El  
345 Niño event, cool and dry conditions in the boreal summer (yr0) inhibited GPP and  
346 TER, whereas warm and wet conditions in the boreal spring and summer (yr1)  
347 enhanced them (Figs. 5a and 4a). In contrast, only the warm and wet conditions in  
348 boreal summer (yr1) enhanced GPP and TER during the CP El Niño event. (Figs. 5c  
349 and 4c). These different configurations of temperature and precipitation variations  
350 during EP and CP El Niños form the different evolutionary characteristics of GPP,  
351 TER, and the resultant  $F_{TA}$ .

352 Detailed regional evolutionary characteristics can be seen from the Hovmöller  
353 diagrams in Fig. 6 and in Supplementary Figs. S3 and S4. Obvious large anomalies in  
354  $F_{TA}$  consistently occurred from 20°N to 40°S during EP and CP El Niños (Figs. 6c and  
355 6f), consistent with the above analyses (Figs. 4b and 4d). Moreover, there was a clear  
356 anomalous carbon uptake between 30°S and 20°N during the period from January  
357 (yr0) to June (yr0) during the EP El Niño (Fig. 6c). This uptake corresponded to the  
358 negative precursor (Figs. 3b and 4b). This anomalous carbon uptake comparably came  
359 from the three continents (Supplementary Figs. S3 a–c). Biological process analyses  
360 indicated that GPP dominated between 5°N and 20°N, and between 30°S and 15°S  
361 (Supplementary Fig. S4a), which was related to the increased amount of precipitation  
362 (Fig. 6b). In contrast, TER dominated between 15°S and 5°N (Supplementary Fig.  
363 S4b), largely due to the colder temperatures (Fig. 6a). Conversely, the strongest  
364 anomalous carbon releases occurred between the equator and 20°N during the period

365 from February (yr1) to August (yr1) during the EP El Niño (Fig. 6c). The largest  
366 contribution to these anomalous carbon releases came from the South America  
367 (Supplementary Fig. S3c). Both GPP and TER showed the anomalous decreases  
368 (Supplementary Figs. S4a and S4b), and stronger decrease in GPP than in TER made  
369 the anomalous carbon releases here (Fig. 6c). Low precipitation (with a few months of  
370 delayed dry conditions; Fig. 6b) and warm temperatures (Fig. 6a) inhibited GPP,  
371 causing the positive  $F_{TA}$  anomaly (Fig. 6c). In contrast, significant carbon releases  
372 were found between 10°N and 20°S from September (yr0) to September (yr1) during  
373 the CP El Niño (Fig. 6f). More specifically, these clear carbon releases largely  
374 originated from South America and tropical Asia (Supplementary Figs. S3 d–f). TER  
375 dominated between 15°S and 10°N during the period from January (yr1) to September  
376 (yr1), and other regions and periods were dominated by GPP (Supplementary Figs.  
377 S4c and S4d). Widespread dry and warm conditions (Figs. 6d and e) effectively  
378 explained these GPP and TER anomalies, as well as the resultant  $F_{TA}$  behavior. For  
379 more detailed information on the other regions, refer to Supplementary Figs. S3 and  
380 S4.

381

#### 382 **4 Discussion**

383 El Niño shows large diversity in individual events (Capotondi et al., 2015), thereby  
384 creating large uncertainties in composite analyses (Figs. 3–5). Four EP El Niño events  
385 during the past five decades were selected for this study to research their effects on  
386 interannual carbon cycle variability (Table 1). Due to the small number of samples

387 and large inter-event spread (Supplementary Fig. S5), the statistical significance of  
388 the composite analyses will need to be further evaluated with upcoming EP El Niño  
389 events occurring in the future. However, cross-correlation analyses between the  
390 long-term CGR (or  $F_{TA}$ ) and the Niño Index have shown that the responses of CGR  
391 (or  $F_{TA}$ ) lag ENSO by a few months (Zeng et al., 2005; Wang et al., 2016; Wang et al.,  
392 2013). This phenomenon can be clearly detected in the EP El Niño composite (Fig.  
393 3b). Therefore, the composite analyses in this study can still give us some insight into  
394 the interannual variability of the global carbon cycle.

395 Another caveat is that the TRENDY models seemed to underestimate the amplitude of  
396 the  $F_{TA}$  anomaly during the extreme EP El Niño events (Fig. 1b). This  
397 underestimation of  $F_{TA}$  may partially result from a bias in the estimation of carbon  
398 releases induced by wildfires. As expected, the carbon releases induced by wildfires  
399 in such 1997/98 strong El Niño event played an important role in global carbon  
400 variations (van der Werf et al., 2004; Chen et al., 2017) (Supplementary Fig. S6).  
401 However, some TRENDY models (ISAM, JULES, and OCN) do not include a fire  
402 module to explicitly simulate the carbon releases induced by wildfires (Table 1), and  
403 those TRENDY models that do contain a fire module generally underestimate the  
404 effects of wildfires. For instance, VISIT and JSBACH clearly underestimated the  
405 carbon flux anomaly induced by wildfires during the 1997/98 EP El Niño event  
406 (Supplementary Fig. S6).

407 The recent extreme 2015/16 El Niño event was not included in this study, because the

408 TRENDY v4 datasets covered the time span from 1860 to 2014. As shown in Wang et  
409 al. (2018), the behavior of the MLO CGR in the 2015/16 El Niño resembled the  
410 composite result of the CP El Niño events (Fig. 3d). But the 2015/16 El Niño event  
411 had the extreme positive SSTA both over the central and eastern Pacific. Its equatorial  
412 eastern Pacific SSTA exceeded +2.0 K, comparable to the historical extreme El Niño  
413 events (e.g. 1982/83, 1997/98); the central Pacific SSTA marked the warmest event  
414 since the modern observation (Thomalla and Boyland, 2017). Therefore, the 2015/16  
415 El Niño event evolved not only in a similar fashion to the EP El Niño dynamics that  
416 rely on the basin-wide thermocline variations, but also in a similar fashion to the CP  
417 El Niño dynamics that rely on the subtropical forcing (Paek et al., 2017; Palmeiro et  
418 al., 2017). The 2015/16 extreme El Niño event can be treated as the strongest mixed  
419 EP and CP El Niño that caused different climate anomalies compared with the  
420 extreme 1997/98 El Niño (Paek et al., 2017; Palmeiro et al., 2017), which had  
421 contrasting terrestrial and oceanic carbon cycle responses (Wang et al., 2018; Liu et  
422 al., 2017; Chatterjee et al., 2017).

423 As above mentioned, when finalizing our paper, we noted the publication of Chylek et  
424 al. (2018) who also focused on interannual atmospheric CO<sub>2</sub> variability during EP and  
425 CP El Niño events. We here simply illustrated some differences and similarities. In  
426 the method of the identification of EP and CP El Niño events, Chylek et al. (2018)  
427 took the Niño1+2 index and Niño4 index to categorize El Niño events, while we  
428 adopted the results of Yu et al. (2012), based on the consensus of three different

429 identification methods, and additionally excluded the events that coincided with  
430 volcanic eruptions. The different methods made some differences in the identification  
431 of EP and CP El Niño events. Chylek et al. (2018) suggested that the CO<sub>2</sub> rise rate had  
432 different time delay to the tropical near surface air temperature, with the delay of  
433 about 8.5 and 4 months during EP and CP El Niños, respectively. Although we did not  
434 find out the exactly same time delay, we suggested that MLO CGR anomaly showed  
435 the peak duration from December (yr0) to April (yr1) in EP El Niños, and from  
436 October (yr0) to January (yr1) in CP El Niños. Additionally, we suggested the  
437 differences of MLO CGR anomaly in precursors and amplitudes during EP and CP El  
438 Niños. Furthermore, we revealed their terrestrial mechanisms based on the inversion  
439 results and the TRENDY multi-model historical simulations.

440

## 441 **5 Concluding Remarks**

442 In this study, we investigate the different impacts of EP and CP El Niño events on the  
443 interannual carbon cycle variability in terms of the composite analysis, based on the  
444 long-term MLO CGR and TRENDY multi-model simulations. We suggest that there  
445 are three clear differences in evolutions of the MLO CGR during EP and CP El Niños  
446 in terms of their precursor, amplitude, and duration of the peak. Specifically, the MLO  
447 CGR anomaly was negative in boreal spring (yr0) during EP El Niño events, while it  
448 was neutral during CP El Niño events. Additionally, the amplitude of the CGR  
449 anomaly was generally larger during EP El Niño events than during CP El Niño

450 events. Also, the duration of the MLO CGR peak during EP El Niño events occurred  
451 from December (yr0) to April (yr1), while it peaked from October (yr0) to January  
452 (yr1) during CP El Niño events.

453 The TRENDY multi-model simulated global  $F_{TA}$  anomalies were able to capture these  
454 characteristics. Further analysis indicated that the  $F_{TA}$  anomalies over the Trop+SH  
455 made the largest contribution to the global  $F_{TA}$  anomalies during these two types of El  
456 Niño events, in which GPP anomalies, rather than TER anomalies, generally  
457 dominated the evolutions of the  $F_{TA}$  anomalies. Regionally, during EP El Niño events,  
458 clear anomalous carbon uptake occurred between 30°S and 20°N during the period  
459 from January (yr0) to June (yr0), corresponding to the negative precursor. This was  
460 primarily caused by more precipitation and colder temperatures. The strongest  
461 anomalous carbon releases happened between the equator and 20°N during the period  
462 from February (yr1) to August (yr1), largely due to the reduced GPP induced by low  
463 precipitation and warm temperatures. In contrast, clear carbon releases existed  
464 between 10°N and 20°S from September (yr0) to September (yr1) during CP El Niño  
465 events, which were caused by widespread dry and warm climate conditions.

466 Some studies (Yeh et al., 2009; Ashok and Yamagata, 2009) have suggested that the  
467 CP El Niño has become or will be more frequent under global warming compared  
468 with the EP El Niño. Because of these different behaviors of the interannual carbon  
469 cycle variability during the two types of El Niños, this shift of El Niño types will alter  
470 the response patterns of interannual terrestrial carbon cycle variability. This

471 possibility should encourage researchers to perform further studies in the future.

472

473 **Data availability.** The monthly atmospheric CO<sub>2</sub> concentration is from NOAA/ESRL  
474 (<https://www.esrl.noaa.gov/gmd/ccgg/trends/index.html>). The Niño3.4 Index is from  
475 ERSST4 (<http://www.cpc.ncep.noaa.gov/data/indices/ersst4.nino.mth.81-10.ascii>).  
476 Temperature and precipitation are from CRUNCEP v6  
477 ([ftp://nacp.ornl.gov/synthesis/2009/frescati/temp/land\\_use\\_change/original/readme.ht](ftp://nacp.ornl.gov/synthesis/2009/frescati/temp/land_use_change/original/readme.htm)  
478 [m](ftp://nacp.ornl.gov/synthesis/2009/frescati/temp/land_use_change/original/readme.htm)). TRENDY v4 data are available from S. Sitch ([s.a.sitch@exeter.ac.uk](mailto:s.a.sitch@exeter.ac.uk)) upon your  
479 reasonable request.

480

481 **Acknowledgements.** We gratefully acknowledge the TRENDY DGVM community,  
482 as part of the Global Carbon Project, for access to gridded land data and the NOAA  
483 ESRL for the use of Mauna Loa atmospheric CO<sub>2</sub> records. This study was supported  
484 by the National Key R&D Program of China (grant no. 2017YFB0504000 and no.  
485 2016YFA0600204), the Natural Science Foundation of Jiangsu Province, China  
486 (Grant No. BK20160625), and the National Natural Science Foundation of China  
487 (Grant No. 41605039). Andrew Wiltshire was supported by the Joint UK BEIS/Defra  
488 Met Office Hadley Centre Climate Programme (GA01101). We also would like to  
489 thank LetPub for proving linguistic assistance.

490

## 491 **References**

492 Ahlstrom, A., Raupach, M. R., Schurgers, G., Smith, B., Arneth, A., Jung, M.,

493 Reichstein, M., Canadell, J. G., Friedlingstein, P., Jain, A. K., Kato, E., Poulter,  
494 B., Sitch, S., Stocker, B. D., Viovy, N., Wang, Y. P., Wiltshire, A., Zaehle, S., and  
495 Zeng, N.: The dominant role of semi-arid ecosystems in the trend and variability  
496 of the land CO<sub>2</sub> sink, *Science*, 348, 895-899, 10.1126/science.aaa1668, 2015.

497 Ashok, K., Behera, S. K., Rao, S. A., Weng, H., and Yamagata, T.: El Niño Modoki  
498 and its possible teleconnection, *Journal of Geophysical Research*, 112,  
499 10.1029/2006jc003798, 2007.

500 Ashok, K., and Yamagata, T.: CLIMATE CHANGE The El Nino with a difference,  
501 *Nature*, 461, 481-+, 10.1038/461481a, 2009.

502 Bacastow, R. B.: Modulation of atmospheric carbon dioxide by the Southern  
503 Oscillation, *Nature*, 261, 116-118, doi:10.1038/261116a0, 1976.

504 Bousquet, P., Peylin, P., Ciais, P., Le Quere, C., Friedlingstein, P., and Tans, P. P.:  
505 Regional changes in carbon dioxide fluxes of land and oceans since 1980,  
506 *Science*, 290, 1342-1346, Doi 10.1126/Science.290.5495.1342, 2000.

507 Capotondi, A., Wittenberg, A. T., Newman, M., Di Lorenzo, E., Yu, J.-Y., Braconnot,  
508 P., Cole, J., Dewitte, B., Giese, B., Guilyardi, E., Jin, F.-F., Karnauskas, K.,  
509 Kirtman, B., Lee, T., Schneider, N., Xue, Y., and Yeh, S.-W.: Understanding  
510 ENSO Diversity, *B Am Meteorol Soc*, 96, 921-938, 10.1175/bams-d-13-00117.1,  
511 2015.

512 Chatterjee, A., Gierach, M. M., Sutton, A. J., Feely, R. A., Crisp, D., Eldering, A.,  
513 Gunson, M. R., O'Dell, C. W., Stephens, B. B., and Schimel, D. S.: Influence of

514 El Nino on atmospheric CO<sub>2</sub> over the tropical Pacific Ocean: Findings from  
515 NASA's OCO-2 mission, *Science*, 358, 10.1126/science.aam5776, 2017.

516 Chen, Y., Morton, D. C., Andela, N., van der Werf, G. R., Giglio, L., and Randerson, J.  
517 T.: A pan-tropical cascade of fire driven by El Niño/Southern Oscillation, *Nature*  
518 *Climate Change*, 7, 906-911, 10.1038/s41558-017-0014-8, 2017.

519 Chylek, P., Tans, P., Christy, J., and Dubey, M. K.: The carbon cycle response to two  
520 El Nino types: an observational study, *Environmental Research Letters*, 13,  
521 10.1088/1748-9326/aa9c5b, 2018.

522 Clark, D. B., Mercado, L. M., Sitch, S., Jones, C. D., Gedney, N., Best, M. J., Pryor,  
523 M., Rooney, G. G., Essery, R. L. H., Blyth, E., Boucher, O., Harding, R. J.,  
524 Huntingford, C., and Cox, P. M.: The Joint UK Land Environment Simulator  
525 (JULES), model description - Part 2: Carbon fluxes and vegetation dynamics,  
526 *Geosci Model Dev*, 4, 701-722, 10.5194/gmd-4-701-2011, 2011.

527 Cox, P. M., Pearson, D., Booth, B. B., Friedlingstein, P., Huntingford, C., Jones, C. D.,  
528 and Luke, C. M.: Sensitivity of tropical carbon to climate change constrained by  
529 carbon dioxide variability, *Nature*, 494, 341-344, 10.1038/nature11882, 2013.

530 Feely, R. A., Boutin, J., Cosca, C. E., Dandonneau, Y., Etcheto, J., Inoue, H. Y., Ishii,  
531 M., Le Quere, C., Mackey, D. J., McPhaden, M., Metzl, N., Poisson, A., and  
532 Wanninkhof, R.: Seasonal and interannual variability of CO<sub>2</sub> in the equatorial  
533 Pacific, *Deep-Sea Res Pt II*, 49, 2443-2469, Pii S0967-0645(02)00044-9, Doi  
534 10.1016/S0967-0645(02)00044-9, 2002.

535 Gu, G. J., and Adler, R. F.: Precipitation and Temperature Variations on the  
536 Interannual Time Scale: Assessing the Impact of ENSO and Volcanic Eruptions,  
537 Journal of Climate, 24, 2258-2270, Doi 10.1175/2010jcli3727.1, 2011.

538 Huang, B., Banzon, V. F., Freeman, E., Lawrimore, J., Liu, W., Peterson, T. C., Smith,  
539 T. M., Thorne, P. W., Woodruff, S. D., and Zhang, H.-M.: Extended  
540 Reconstructed Sea Surface Temperature Version 4 (ERSST.v4). Part I: Upgrades  
541 and Intercomparisons, Journal of Climate, 28, 911-930,  
542 10.1175/jcli-d-14-00006.1, 2015.

543 Jain, A. K., Meiyappan, P., Song, Y., and House, J. I.: CO2 emissions from land-use  
544 change affected more by nitrogen cycle, than by the choice of land-cover data,  
545 Global Change Biology, 19, 2893-2906, 10.1111/gcb.12207, 2013.

546 Jones, P. W.: First- and second-order conservative remapping schemes for grids in  
547 spherical coordinates, Mon Weather Rev, 127, 2204-2210, Doi  
548 10.1175/1520-0493(1999)127<2204:Fasocr>2.0.Co;2, 1999.

549 Jung, M., Reichstein, M., Schwalm, C. R., Huntingford, C., Sitch, S., Ahlstrom, A.,  
550 Arneeth, A., Camps-Valls, G., Ciais, P., Friedlingstein, P., Gans, F., Ichii, K., Jain,  
551 A. K., Kato, E., Papale, D., Poulter, B., Raduly, B., Rodenbeck, C., Tramontana,  
552 G., Viovy, N., Wang, Y. P., Weber, U., Zaehle, S., and Zeng, N.: Compensatory  
553 water effects link yearly global land CO<sub>2</sub> sink changes to temperature, Nature,  
554 541, 516-520, 10.1038/nature20780, 2017.

555 Kao, H.-Y., and Yu, J.-Y.: Contrasting Eastern-Pacific and Central-Pacific Types of

556 ENSO, *Journal of Climate*, 22, 615-632, 10.1175/2008jcli2309.1, 2009.

557 Kato, E., Kinoshita, T., Ito, A., Kawamiya, M., and Yamagata, Y.: Evaluation of  
558 spatially explicit emission scenario of land-use change and biomass burning  
559 using a process-based biogeochemical model, *Journal of Land Use Science*, 8,  
560 104-122, 10.1080/1747423x.2011.628705, 2013.

561 Keeling, C. D., and Revelle, R.: Effects of El-Nino Southern Oscillation on the  
562 Atmospheric Content of Carbon-Dioxide, *Meteoritics*, 20, 437-450, 1985.

563 Keeling, C. D., Whorf, T. P., Wahlen, M., and Vanderpligt, J.: Interannual Extremes  
564 in the Rate of Rise of Atmospheric Carbon-Dioxide since 1980, *Nature*, 375,  
565 666-670, Doi 10.1038/375666a0, 1995.

566 Keller, K. M., Lienert, S., Bozbiyik, A., Stocker, T. F., Churakova, O. V., Frank, D. C.,  
567 Klesse, S., Koven, C. D., Leuenberger, M., Riley, W. J., Saurer, M., Siegwolf, R.,  
568 Weigt, R. B., and Joos, F.: 20th century changes in carbon isotopes and water-use  
569 efficiency: tree-ring-based evaluation of the CLM4.5 and LPX-Bern models,  
570 *Biogeosciences*, 14, 2641-2673, 10.5194/bg-14-2641-2017, 2017.

571 Kim, J.-S., Kug, J.-S., Yoon, J.-H., and Jeong, S.-J.: Increased Atmospheric CO<sub>2</sub>  
572 Growth Rate during El Niño Driven by Reduced Terrestrial Productivity in the  
573 CMIP5 ESMs, *Journal of Climate*, 29, 8783-8805, 10.1175/jcli-d-14-00672.1,  
574 2016.

575 Kim, J.-S., Kug, J.-S., and Jeong, S.-J.: Intensification of terrestrial carbon cycle  
576 related to El Niño–Southern Oscillation under greenhouse warming, *Nature*

577           Communications, 8, 10.1038/s41467-017-01831-7, 2017.

578   Lee, K., Wanninkhof, R., Takahashi, T., Doney, S. C., and Feely, R. A.: Low  
579           interannual variability in recent oceanic uptake of atmospheric carbon dioxide,  
580           Nature, 396, 155-159, Doi 10.1038/24139, 1998.

581   Liu, J., Bowman, K. W., Schimel, D. S., Parazoo, N. C., Jiang, Z., Lee, M., Bloom, A.  
582           A., Wunch, D., Frankenberg, C., Sun, Y., O'Dell, C. W., Gurney, K. R.,  
583           Menemenlis, D., Gierach, M., Crisp, D., and Eldering, A.: Contrasting carbon  
584           cycle responses of the tropical continents to the 2015-2016 El Nino, Science, 358,  
585           10.1126/science.aam5690, 2017.

586   Mercado, L. M., Bellouin, N., Sitch, S., Boucher, O., Huntingford, C., Wild, M., and  
587           Cox, P. M.: Impact of changes in diffuse radiation on the global land carbon sink,  
588           Nature, 458, 1014-U1087, Doi 10.1038/Nature07949, 2009.

589   Mudelsee, M.: Climate Time Series Analysis: Classical Statistical and Bootstrap  
590           Methods, Springer, Dordrecht, 2010.

591   Oleson, K., Lawrence, D., Bonan, G., Drewniak, B., Huang, M., Koven, C., Levis, S.,  
592           Li, F., Riley, W., Subin, Z., Swenson, S. C., Thorne, P. W., Bozbiyik, A., Fisher,  
593           R., Heald, C., Kluzek, E., Lamarque, J. F., Lawrence, P. J., Leung, L. R.,  
594           Lipscomb, W. H., Muszala, S., Ricciuto, D. M., Sacks, W. J., Tang, J., and Yang,  
595           Z.: Technical Description of version 4.5 of the Community Land Model (CLM),  
596           NCAR, 2013.

597   Paek, H., Yu, J.-Y., and Qian, C.: Why were the 2015/2016 and 1997/1998 extreme El

598 Nino different?, *Geophys Res Lett*, 44, 10.1002/2016GL071515, 2017.

599 Palmeiro, F. M., Iza, M., Barriopedro, D., Calvo, N., and García-Herrera, R.: The  
600 complex behavior of El Niño winter 2015-2016, *Geophys Res Lett*, 44,  
601 2902-2910, 10.1002/2017gl072920, 2017.

602 Patra, P. K., Maksyutov, S., Ishizawa, M., Nakazawa, T., Takahashi, T., and Ukita, J.:  
603 Interannual and decadal changes in the sea-air CO<sub>2</sub> flux from atmospheric CO<sub>2</sub>  
604 inverse modeling, *Global Biogeochemical Cycles*, 19, Artn Gb4013, Doi  
605 10.1029/2004gb002257, 2005.

606 Peylin, P., Law, R. M., Gurney, K. R., Chevallier, F., Jacobson, A. R., Maki, T., Niwa,  
607 Y., Patra, P. K., Peters, W., Rayner, P. J., Rödenbeck, C., van der Laan-Luijkx, I.  
608 T., and Zhang, X.: Global atmospheric carbon budget: results from an ensemble  
609 of atmospheric CO<sub>2</sub> inversions, *Biogeosciences*, 10, 6699-6720,  
610 10.5194/bg-10-6699-2013, 2013.

611 Piao, S., Sitch, S., Ciais, P., Friedlingstein, P., Peylin, P., Wang, X., Ahlström, A.,  
612 Anav, A., Canadell, J. G., Cong, N., Huntingford, C., Jung, M., Levis, S., Levy, P.  
613 E., Li, J., Lin, X., Lomas, M. R., Lu, M., Luo, Y., Ma, Y., Myneni, R. B., Poulter,  
614 B., Sun, Z., Wang, T., Viovy, N., Zaehle, S., and Zeng, N.: Evaluation of  
615 terrestrial carbon cycle models for their response to climate variability and to  
616 CO<sub>2</sub> trends, *Global Change Biology*, 2117–2132, 10.1111/gcb.12187, 2013.

617 Qian, H., Joseph, R., and Zeng, N.: Response of the terrestrial carbon cycle to the El  
618 Nino-Southern Oscillation, *Tellus Series B-Chemical and Physical Meteorology*,

619 60, 537-550, Doi 10.1111/J.1600-0889.2008.00360.X, 2008.

620 Reick, C. H., Raddatz, T., Brovkin, V., and Gayler, V.: Representation of natural and  
621 anthropogenic land cover change in MPI-ESM, *J Adv Model Earth Sy*, 5,  
622 459-482, 10.1002/jame.20022, 2013.

623 Rodenbeck, C., Houweling, S., Gloor, M., and Heimann, M.: CO2 flux history  
624 1982-2001 inferred from atmospheric data using a global inversion of  
625 atmospheric transport, *Atmos. Chem. Phys.*, 3, 1919-1964,  
626 10.5194/acp-3-1919-2003, 2003.

627 Sarmiento, J. L., Gloor, M., Gruber, N., Beaulieu, C., Jacobson, A. R., Fletcher, S. E.  
628 M., Pacala, S., and Rodgers, K.: Trends and regional distributions of land and  
629 ocean carbon sinks, *Biogeosciences*, 7, 2351-2367, 2010.

630 Schwalm, C. R.: Does terrestrial drought explain global CO2 flux anomalies induced  
631 by El Nino?, *Biogeosciences*, 8, 2493-2506, 2011.

632 Sitch, S., Friedlingstein, P., Gruber, N., Jones, S. D., Murray-Tortarolo, G., Ahlström,  
633 A., Doney, S. C., Graven, H., Heinze, C., Huntingford, C., Levis, S., Levy, P. E.,  
634 Lomas, M., Poulter, B., Viovy, N., Zaehle, S., Zeng, N., Arneth, A., Bonan, G.,  
635 Bopp, L., Canadell, J. G., Chevallier, F., Ciais, P., Ellis, R., Gloor, M., Peylin, P.,  
636 Piao, S. L., Le Quéré, C., Smith, B., Zhu, Z., and Myneni, R.: Recent trends and  
637 drivers of regional sources and sinks of carbon dioxide, *Biogeosciences*, 12,  
638 653-679, 10.5194/bg-12-653-2015, 2015.

639 Thomalla, F., and Boyland, M.: Enhancing resilience to extreme climate events:

640 Lessons from the 2015-2016 El Niño event in Asia and the Pacific. UNESCAP,  
641 Bangkok.

642 van der Werf, G. R., Randerson, J. T., Collatz, G. J., Giglio, L., Kasibhatla, P. S.,  
643 Arellano, A. F., Jr., Olsen, S. C., and Kasischke, E. S.: Continental-scale  
644 partitioning of fire emissions during the 1997 to 2001 El Niño/La Niña period,  
645 Science, 303, 73-76, 10.1126/science.1090753, 2004.

646 Wang, J., Zeng, N., and Wang, M.: Interannual variability of the atmospheric CO<sub>2</sub>  
647 growth rate: roles of precipitation and temperature, Biogeosciences, 13,  
648 2339-2352, 10.5194/bg-13-2339-2016, 2016.

649 Wang, J., Zeng, N., Wang, M., Jiang, F., Wang, H., and Jiang, Z.: Contrasting  
650 terrestrial carbon cycle responses to the 1997/98 and 2015/16 extreme El Niño  
651 events, Earth System Dynamics, 9, 1-14, 10.5194/esd-9-1-2018, 2018.

652 Wang, W., Ciais, P., Nemani, R., Canadell, J. G., Piao, S., Sitch, S., White, M. A.,  
653 Hashimoto, H., Milesi, C., and Myneni, R. B.: Variations in atmospheric CO<sub>2</sub>  
654 growth rates coupled with tropical temperature, PNAS, 110, 13061-13066,  
655 10.1073/pnas.1314920110, 2013.

656 Wang, X., Piao, S., Ciais, P., Friedlingstein, P., Myneni, R. B., Cox, P., Heimann, M.,  
657 Miller, J., Peng, S., Wang, T., Yang, H., and Chen, A.: A two-fold increase of  
658 carbon cycle sensitivity to tropical temperature variations, Nature, 506, 212-215,  
659 10.1038/nature12915, 2014.

660 Wei, Y., Liu, S., Huntzinger, D. N., Michalak, A. M., Viovy, N., Post, W. M., Schwalm,

661 C. R., Schaefer, K., Jacobson, A. R., Lu, C., Tian, H., Ricciuto, D. M., Cook, R.  
662 B., Mao, J., and Shi, X.: The North American Carbon Program Multi-scale  
663 Synthesis and Terrestrial Model Intercomparison Project – Part 2: Environmental  
664 driver data, *Geosci Model Dev*, 7, 2875-2893, 10.5194/gmd-7-2875-2014, 2014.

665 Weng, H., Ashok, K., Behera, S. K., Rao, S. A., and Yamagata, T.: Impacts of recent  
666 El Niño Modoki on dry/wet conditions in the Pacific rim during boreal summer,  
667 *Climate Dynamics*, 29, 113-129, 10.1007/s00382-007-0234-0, 2007.

668 Weng, H., Behera, S. K., and Yamagata, T.: Anomalous winter climate conditions in  
669 the Pacific rim during recent El Niño Modoki and El Niño events, *Climate*  
670 *Dynamics*, 32, 663-674, 10.1007/s00382-008-0394-6, 2009.

671 Yeh, S. W., Kug, J. S., Dewitte, B., Kwon, M. H., Kirtman, B. P., and Jin, F. F.: El  
672 Niño in a changing climate, *Nature*, 461, 511-514, 10.1038/nature08316, 2009.

673 Yu, J.-Y., Zou, Y., Kim, S. T., and Lee, T.: The changing impact of El Niño on US  
674 winter temperatures, *Geophys Res Lett*, 39, 10.1029/2012gl052483, 2012.

675 Zaehle, S., and Friend, A. D.: Carbon and nitrogen cycle dynamics in the O-CN land  
676 surface model: 1. Model description, site-scale evaluation, and sensitivity to  
677 parameter estimates, *Global Biogeochemical Cycles*, 24, Artn Gb1005, Doi  
678 10.1029/2009gb003521, 2010.

679 Zeng, N., Mariotti, A., and Wetzel, P.: Terrestrial mechanisms of interannual  
680 CO<sub>2</sub> variability, *Global Biogeochemical Cycles*, 19, GB1016,  
681 10.1029/2004gb002273, 2005.

682 Zhang, Y., Xiao, X., Guanter, L., Zhou, S., Ciais, P., Joiner, J., Sitch, S., Wu, X.,  
683 Nabel, J., Dong, J., Kato, E., Jain, A. K., Wiltshire, A., and Stocker, B. D.:  
684 Precipitation and carbon-water coupling jointly control the interannual  
685 variability of global land gross primary production, *Sci Rep*, 6, 39748,  
686 10.1038/srep39748, 2016.

687

688

689

690

691

692

693

694

695

696

697

698

699

700

701

702

703

704

705

706

## Tables and Figures

707 Table 1 TRENDY models used in this study.

No.	Model	Resolution (lat×lon)	Fire Simulation	References
1	CLM4.5	0.94°×1.25°	yes	Oleson et al., 2013
2	ISAM	0.5°×0.5°	no	Jain et al., 2013
3	JSBACH	1.875°×1.875°	yes	Reick et al., 2013
4	JULES	1.6°×1.875°	no	Clark et al., 2011
5	LPX-Bern	1°×1°	yes	Keller et al., 2017
6	OCN	0.5°×0.5°	no	Zaehle et al., 2010
7	VEGAS	0.5°×0.5°	yes	Zeng et al., 2005
8	VISIT	0.5°×0.5°	yes	Kato et al., 2013

708

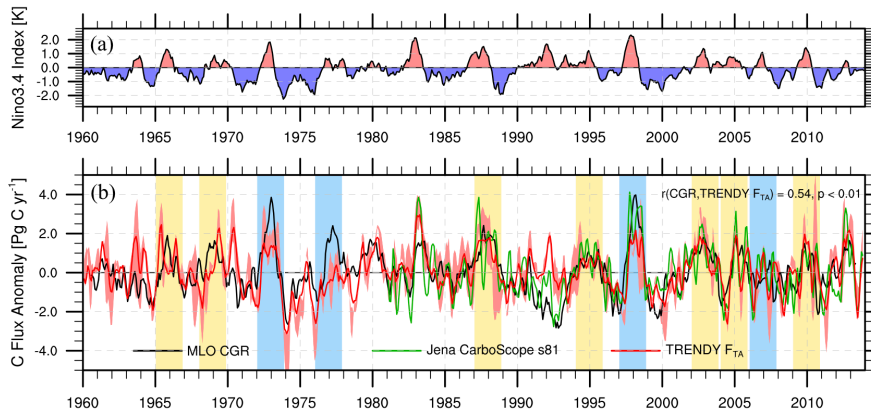
709 Table 2 Eastern Pacific (EP) and Central Pacific (CP) El Niño events used in this  
710 study, as identified by a majority consensus of three methods.

EP El Niño	CP El Niño
1972/73	1965/66
1976/77	1968/69
1997/98	1987/88
2006/07	1994/95
	2002/03
	2004/05
	2009/10

711

712

713



714

715 Figure 1. Interannual variability in the Niño3.4 Index and the carbon cycle. (a)

716 Niño3.4. (b) Mauna Loa (MLO) CO<sub>2</sub> growth rate (CGR, black line), as well as

717 TRENDY multi-model median (red line) and Jena inversion (green line) of the global

718 land–atmosphere carbon flux ( $F_{TA}$ , positive value means into the atmosphere, units in

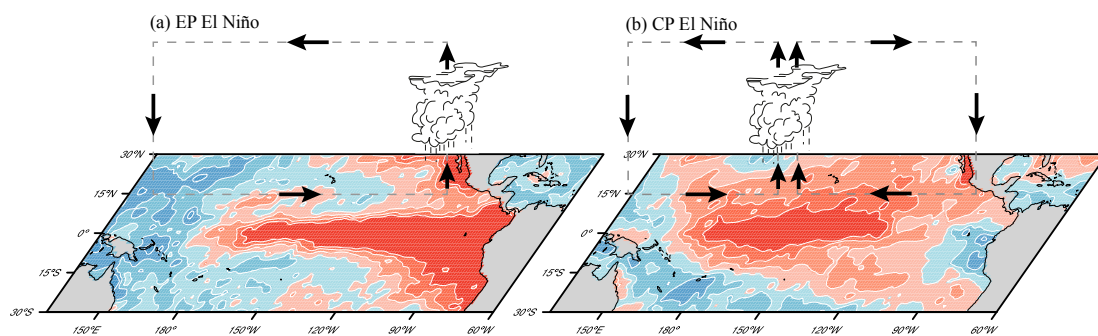
719  $\text{Pg C yr}^{-1}$ ), which were further smoothed by the 3-month running average. The light

720 red shaded represents the area between the 5% and 95% percentiles of the TRENDY

721 simulations. The bars represent the El Niño events selected for this study, with the EP

722 El Niño in blue and the CP El Niño in yellow.

723

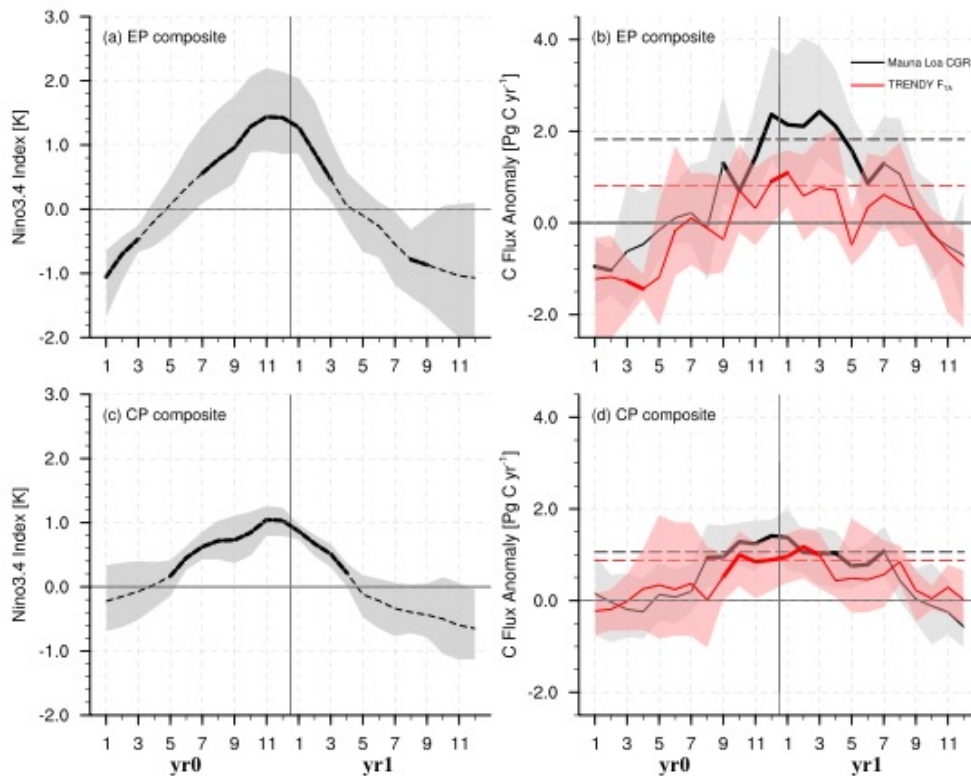


724

725 Figure 2. Schematic diagram of the two types of El Niños. (a) sea surface temperature

726 anomaly (SSTA) over the tropical Pacific associated with the anomalous Walker

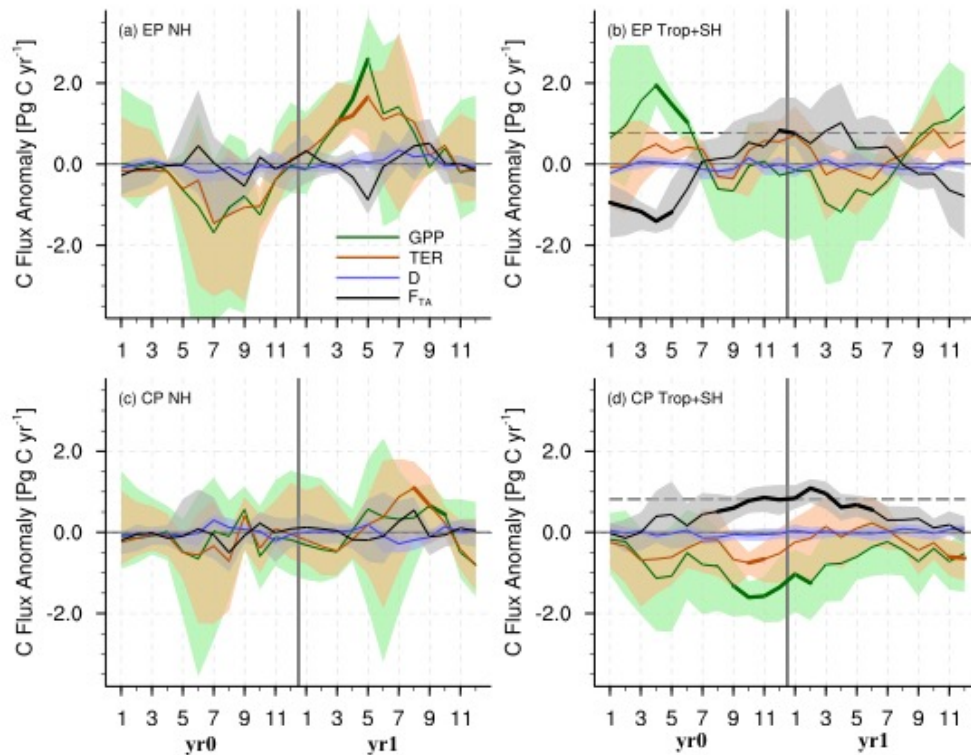
727 Circulation in an EP El Niño. (b) SSTA with two cells of the anomalous Walker  
 728 Circulation in a CP El Niño. Red colors indicate warming, and blue colors indicate  
 729 cooling. Vectors denote the wind directions.  
 730



731  
 732 Figure 3. Composites of El Niño and the corresponding carbon flux anomaly ( $\text{Pg C}$   
 733  $\text{yr}^{-1}$ ). (a) The Niño3.4 Index composite during EP El Niño events. (b) Corresponding  
 734 MLO CGR and TRENDY v4 global  $F_{\text{TA}}$  composite during EP El Niño events. (c) The  
 735 Niño3.4 Index composite during CP El Niño events. (d) Corresponding MLO CGR  
 736 and TRENDY v4 global  $F_{\text{TA}}$  composite during CP El Niño events. The shaded area  
 737 denotes the 95% confidence intervals of the variables in the composite, derived from  
 738 1000 bootstrap estimates. The bold lines indicate the significance above the 80% level

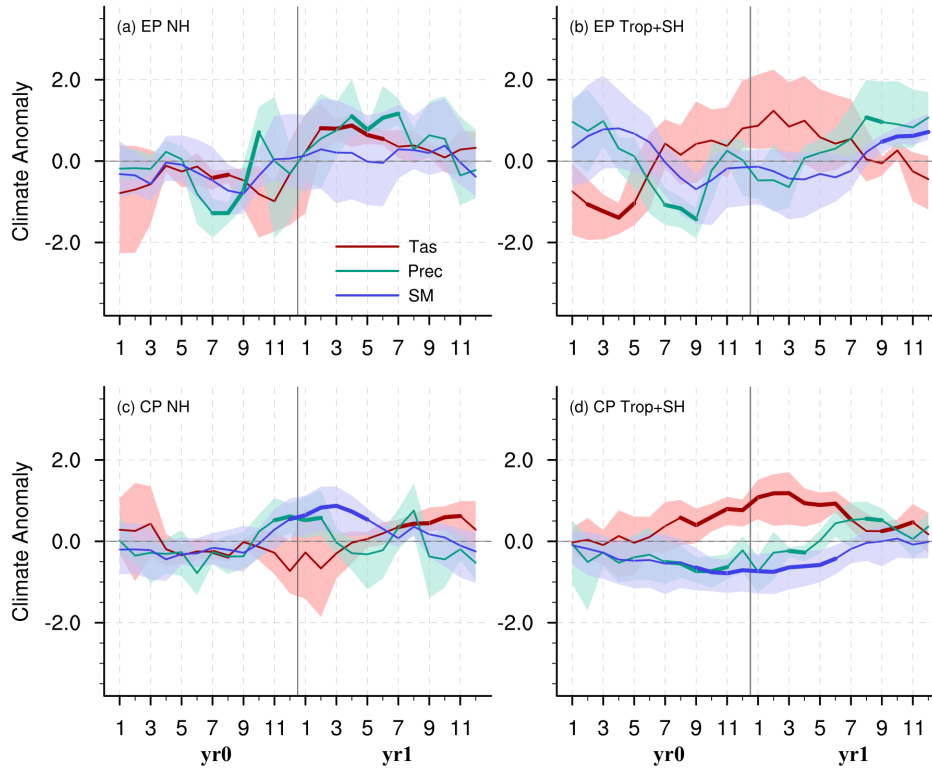
739 estimated by the Student's *t*-test. The black and red dash lines in b and d represent the  
 740 thresholds of the peak duration (75% of the maximum CGR or  $F_{TA}$  anomaly).

741



742

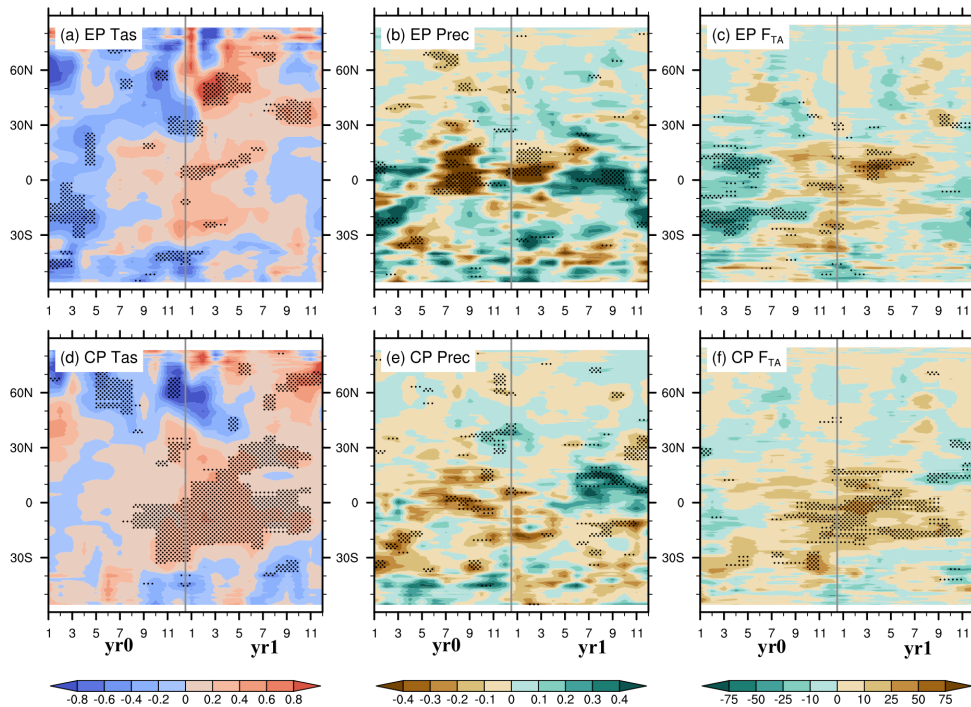
743 Figure 4. Composites of anomalies in the TRENDY  $F_{TA}$  (black lines), gross primary  
 744 productivity (GPP, green lines), terrestrial ecosystem respiration (TER, brown lines),  
 745 and the carbon flux caused by disturbances (D, blue lines) during two types of El  
 746 Niños over the extratropical northern hemisphere (NH, 23°N–90°N) and the tropics  
 747 and extratropical southern hemisphere (Trop+SH, 60°S–23°S). The shaded area  
 748 denotes the 95% confidence intervals of the variables in the composite, derived from  
 749 1000 bootstrap estimates. The bold lines indicate the significance above the 80% level  
 750 estimated by the Student's *t*-test. The black dash lines in b and d represent the  
 751 thresholds of the peak duration.



752

753 Figure 5. Composites of the standardized land surface air temperature (Tas, red lines),  
 754 precipitation (green lines), and TRENDY simulated soil moisture content (SM, blue  
 755 lines) anomalies in two types of El Niños over the NH, Trop+SH. Shaded area  
 756 denotes the 95% confidence intervals of the variables in the composite, derived in  
 757 1000 bootstrap estimates. The bold lines indicate the significance above the 80% level  
 758 estimated by Student's *t*-test.

759



760

761 Figure 6. Hovmöller diagrams of the anomalies in climate variables and the  $F_{TA}$

762 (averaged from  $180^{\circ}W$  to  $180^{\circ}E$ ) during EP and CP El Niño events. (a and d) surface

763 air temperature anomalies over land (units: K); (b and e) precipitation anomalies over

764 land (units:  $\text{mm d}^{-1}$ ); (c and f) TRENDY simulated  $F_{TA}$  anomalies (units:  $\text{g C m}^{-2} \text{yr}^{-1}$ )

765 during EP and CP El Niño events. The dotted areas indicate the significance above the

766 80% level as estimated using the Student's  $t$ -test.

767

768